Catalysis Letters (2019) 149:1154–1166
https://doi.org/10.1007/s10562-019-02704-y

# Z-Scheme $Ag_3PO_4$/g-$C_3N_4$ Nanocomposites for Robust Cocatalyst-Free Photocatalytic $H_2$ Evolution Under Visible Light Irradiation

**Dan Long[1] · Hailong Dou[1] · Xi Rao[1] · Zhiqian Chen[1] · Yongping Zhang[1]**

Received: 15 November 2018 / Accepted: 4 February 2019 / Published online: 20 February 2019


## Abstract

$Ag_3PO_4$/g-$C_3N_4$ nanocomposite photocatalysts were synthesized by calcining the mixture of urea and trace amount of $Ag_3PO_4$ microcrystals at 600 °C, in which $Ag_3PO_4$ nanoparticles with size of 20–30 nm were wrapped with g-$C_3N_4$ layers. The obtained $Ag_3PO_4$/g-$C_3N_4$ composites exhibited efficient utilization of visible light and separation of photoinduced electron–hole pairs, resulting in enhanced photocatalytic activity for $H_2$ evolution. The optimum photocatalytic $H_2$ evolution rate under visible light without Pt co-catalyst for 0.04AP-CN composite was 89.4 μmol/h, which is 3.34 times of that of g-$C_3N_4$ (26.7 μmol/h). The $H_2$ evolution rate for 0.04AP-CN with 3 wt% Pt co-catalyst was up to 273.6 μmol/h, which is 2.39 times of that g-$C_3N_4$ (114.4 μmol/h). The performance of $Ag_3PO_4$/g-$C_3N_4$ composite was enhanced significantly due to the synergistic effect of the interface formed between $Ag_3PO_4$ and g-$C_3N_4$.

## Graphical Abstract

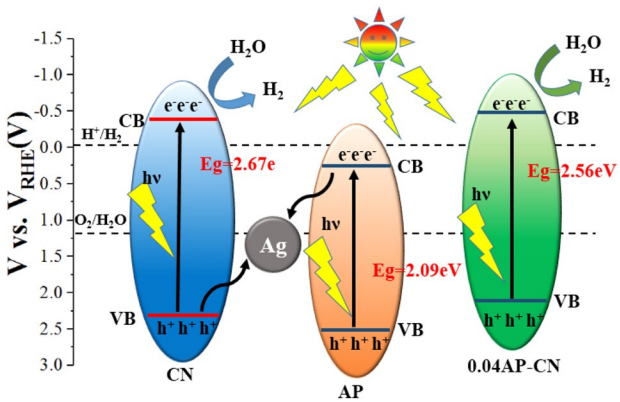


Photocatalytic mechanism of the $Ag_3PO_4$/g-$C_3N_4$ composite

**Keywords** Graphitic carbon nitride · $H_2$ evolution · Visible-light driven photocatalyst · Photocatalysis · Composite photocatalyst

## 1 Introduction

Resource deficiency, energy shortage and environmental deterioration pressed even more grave conditions for human to confront with. Hydrogen energy was generally thought as the ultimately energy resource for its advantages of high combustion calorific value, abundant resources and clean combustion products. Photocatalysis provided certain promising approaches for $H_2$ evolution via water splitting

**Electronic supplementary material** The online version of this article (https://doi.org/10.1007/s10562-019-02704-y) contains supplementary material, which is available to authorized users.

✉ Yongping Zhang
zhangyyping@yahoo.com

[1] Faculty of Materials and Energy, Southwest University, Chongqing 400715, People's Republic of China

and pollutant degradation using solar energy directly and aroused considerable interests for research experts in materials science and chemistry [1–4]. The graphitic carbon nitride (g-$C_3N_4$) is a new metal-free semiconductor with layered structure and suitable band gap of 2.7 eV allowing it to serve as a promising photocatalyst for realizing the hydrogen evolution via water splitting using solar resource conversion [5–9]. Besides its advantages of chemical stability, low-cost precursors and nonmetal photocatalyst, some shortcomings restricted its practical application, such as small specific surface area and rapid recombination of the photogenerated electron–hole pairs. Ever since its emergence as a photocatalyst, lots of research strategies have been proposed to improve its photocatalytic performance by doping metal or non-metal elements, designing appropriate molecular structures, supporting metal nanoparticles, and forming heterojunction with other semiconductors [10–15]. Among all those methods, forming heterojunction with other semiconductors is one of the most effective strategy to improve the separation of photoinduced charge carriers, and enhance the visible light absorption, thus improve the photocatalytic activities. Those reported semiconductors included metal oxide,[16–24] sulfide,[19] halide,[19, 25] carbide, and phosphate, etc.[21–30].

The $Ag_3PO_4$ nanocrystals were studied as a visible light driven photocatalyst for having good oxidation ability to degradate organic pollutants and $O_2$ evolution via water splitting, but lacking the reduction ability enough to reduce water to hydrogen. Silver halide and phosphate are not stable under light irradiation, and Ag nanoparticles may be formed during the photocatalysis process. The surface plasma effect induced by Ag nanoparticles can effectively improve the visible light absorption on the thin surface layer (10 nm), and the charge carrier separation of the photoinduced electron–hole pairs. The size of $Ag_3PO_4$ particles can be reduced significantly through the preparation process of forming the $Ag_3PO_4$/g-$C_3N_4$ composite, enhancing the migration of photoinduced charge carriers. Therefore, the photocatalytic performance was improved by forming $Ag_3PO_4$/g-$C_3N_4$ nanocomposite [28–33]. The reported literatures usually involved the $Ag_3PO_4$/g-$C_3N_4$ composites with $Ag_3PO_4$ fraction of more than 50%, in which $Ag_3PO_4$ acts as a matrix and g-$C_3N_4$ as a solute. Those composite photocatalysts have enhanced performance in degradation of Rhodaming B (RhB), Methyl orange (MO) and conversion of $CO_2$ with g-$C_3N_4$ hybrids with $Ag_3PO_4$. The enhanced photocatalytic activity can be explained using the Z-scheme via $Ag_3PO_4$ and g-$C_3N_4$ heterojunction. We explore the possibility that the $Ag_3PO_4$/g-$C_3N_4$ composite with lower ratio of $Ag_3PO_4$ may have different photocatalytic activities using g-$C_3N_4$ as a matrix since the performance of g-$C_3N_4$ can be enhanced significantly by small amount of compound semiconductors such as NiC and $Ag_2O$ [12, 14].

In this paper, we reported a facile calcination technique to prepare the $Ag_3PO_4$/g-$C_3N_4$ nanocomposites by thermal annealing the mixture of urea and trace amount of $Ag_3PO_4$. The $H_2$ evolution rate of g-$C_3N_4$ was enhanced significantly by introducing a trace amount of $Ag_3PO_4$, and the $H_2$ evolution process was in progress without co-catalyst. The Ag nanoparticles formed under solar light irradiation may act as the combination center for photoinduced electrons and holes, thus enhanced the charge separation in the photocatalyst by forming an efficient Z-scheme photocatalysis system for $H_2$ evolution via water splitting.

## 2 Experimental Details

### 2.1 Synthesis of the Photocatalysts

All the chemicals were of analytical grade and used without further purification.

Pure $Ag_3PO_4$ was prepared via an ion exchange method. 0.4 M aqueous solution of silver nitrate was added to a beaker and 0.15 M aqueous solution of sodium acetate was added dropwise under continuous stirring for 2 h at room temperature. Then 0.1 M solution of $KH_2PO_4$ added to above-mentioned solution under stirring for 3 h. The solution was centrifuged and the solid product was washed three times with distilled water and ethanol and then dried in an oven at 60 °C. The obtained $Ag_3PO_4$ microcrystal was marked as AP.

For the preparation of the $Ag_3PO_4$/g-$C_3N_4$ nanocomposite photocatalysts, an appropriate amount (0.01 g, 0.02 g, 0.04 g, 0.06 g, and 0.08 g) of $Ag_3PO_4$ was mixed with 8 g urea, and calcined at 600 °C for 90 min. The obtained yellow products were noted as 0.01AP-CN, 0.02AP-CN, 0.04AP-CN, 0.06AP-CN, and 0.08AP-CN, respectively. The pure g-$C_3N_4$ was prepared by calcified 8 g urea at 600 °C for 90 min, and noted as CN as reference sample.

### 2.2 Characterization

The morphologies of the prepared samples were observed by scanning electron microscope (SEM, JSE-7800F, Jeol), transmission electron microscope (TEM, Libra 200FE, Zeiss), and tapping mode atomic force microscope (AFM, CSPM5500, Being, china). The X-ray diffraction (XRD) patterns were performed to characterized the crystalline structures of the photocatalysts by a Shimadzu XRD7000 instrument with Cu Kα radiation ($\lambda = 1.5418$ Å). Fourier transform infrared (FTIR) was measured using a Perkin Elmer (Frontier) spectroscopy instrument in KBr pellets. X-ray photoelectron spectroscopy (XPS) was carried out to analyze the chemical state and composition on a VG ESCALAB 250 spectrometer with Al Kα radiation ($h\nu = 1486.8$ eV). Ultraviolet–visible (UV–vis)

absorption spectra were performed on U-3310 spectrophotometer (Hitachi, Japan) in the wavelength range of 300 nm to 800 nm. Photoluminescence (PL) spectra were carried out on an F-7000 fluorescence spectrophotometer (Hitachi, Japan) with an excitation wavelength at 273 nm using a 150 W Xe lamp as the excitation source. The Brunauer-Emmett-Teller (BET) specific surface area was characterized by nitrogen adsorption at 77 K with Quadrasorbevo 2QDS-MP-30 (Quantachrome Instruments, USA). The photocurrent measurements were conducted on an Autolab electrochemical workstation (Aut86039) in a standard three-electrode system, using a platinum wire and the saturated Ag/AgCl electrode as the counter electrode and reference electrode, respectively. The working electrode was prepared by coating the catalysts on a 1.8 cm × 1.2 cm fluorine-doped tin oxide (FTO) glass substrate. A 500 W Xe lamp with a light intensity of 113.8 mW/cm$^2$ was used as a light source.

### 2.3 Photocatalytic Hydrogen Evolution

Photocatalytic hydrogen evolution was performed by a full spectrum photocatalysts performance evaluation system (Suncat Instruments Co., China). The reactor was made up a quartz container with highly transparent window in a diameter of 2.5 cm at the bottom. A 500 W Xe lamp (Zolix, Gloria-X500A) with adjustable intensity was used as solar simulator with a 400 nm cutoff filter for the photocatalytic reactions. The reactor with volume of 130 ml was kept at 20 °C and the light intensity was 113.8 mW/cm$^2$. 10 mg of photocatalyst was dispersed in 30 ml water solution with 20 vol% triethanolamine (TEOA) aqueous solution as an electron donor. Prior to irradiation, the reactor was evacuated to high vacuum up to $10^{-8}$ Torr to remove air and filled with argon. The reaction suspension was stirred with a magnetic stirrer under solar irradiation. During the photocatalytic process, 1 ml of the gas sample was withdrawn from the reaction cell at 30 min intervals and the pressure was automatically compensated with argon. The amount of hydrogen evolved was measured with a Shimadzu gas chromatography (GC-2018; Molecular sieve TDX-01, TCD detector, Ar carrier gas) and calibrated with an Agilent 5 ml syringe. The apparent quantum yield (AQY) of the photocatalysts was calculated according to the light absorption and $H_2$ evolution rate as follows:

$$\mathrm{AQY}\% = \frac{\text{number of transfered electrons in reaction}}{\text{number of incident photons}} \times 100 = \frac{2 \times \text{number of evolved } H_2 \text{ molecules}}{\text{number of incident photons}} \times 100$$

## 3 Results and Discussion

### 3.1 Structural and Composition Characterization

Figure 1a showed the XRD patterns of the as-synthesized $Ag_3PO_4$/g-$C_3N_4$ photocalysts with different amount of $Ag_3PO_4$, and the reference samples of the pure g-$C_3N_4$ and $Ag_3PO_4$ particles. The XRD pattern indicated that $Ag_3PO_4$ particles were indexed as body-centered cubic phase (JCPDS No. 06-0505) with good crystallinity. For the pure g-$C_3N_4$ sample, there existed two broad peaks around 27.4° and 13.0°, corresponding to the (002) and (100) diffraction planes, respectively. The (002) plane is attributed to the long-range interplanar stacking of aromatic units with interlayer distance of 0.326 nm; while the (100) plane with weak intensity is associated with the in-plane trigonal nitrogen linked tri-s-triazine motifs with distance of 0.681 nm. For the $Ag_3PO_4$/g-$C_3N_4$ composites, the intrinsic diffraction peaks of g-$C_3N_4$ were observed clearly, indicating that g-$C_3N_4$ structure remained intact via hybridization with $Ag_3PO_4$ nanoparticles. No $Ag_3PO_4$ diffraction peaks could be discerned for the $Ag_3PO_4$/g-$C_3N_4$ composites owing to the low $Ag_3PO_4$ fraction and small particle size. With the increase of $Ag_3PO_4$ component ratio, the peak for (002) plane is shifted to higher 2θ position, which indicated the decreased interlayer distance due to the enhanced interaction of g-$C_3N_4$ layer by intercalating $Ag_3PO_4$. In addition, the diffraction intensity for peak (002) increased and full width at half maxima (FWHM) decreased a little with the increase of $Ag_3PO_4$ amount, indicating improved crystallinity of $Ag_3PO_4$/g-$C_3N_4$ composites. The XRD results showed that small amount of $Ag_3PO_4$ nanoparticles increased the interlayer interaction, facilitating the compact g-$C_3N_4$ with better crystallinity.

The FTIR spectra of $Ag_3PO_4$, g-$C_3N_4$, and $Ag_3PO_4$/g-$C_3N_4$ photocatalysts were shown in Fig. 1b. In the spectrum of g-$C_3N_4$, there exist the broad bands around 3000–3500 cm$^{-1}$, assigning to the stretching mode of N–H. The peak at 810 cm$^{-1}$ is related to the bending mode of the s-triazine ring. The peaks at 1233, 1315, 1400, 1460, 1540 cm$^{-1}$ correspond to the stretching vibrations of the aromatic CN heterocycles. In the spectrum of $Ag_3PO_4$, there exist two peaks at 930 cm$^{-1}$ and 570 cm$^{-1}$, corresponding to the P–O stretching vibrations of $PO_4^{3-}$. No obvious change can be detected for the characteristic IR vibration peaks of g-$C_3N_4$ by adding small amount of $Ag_3PO_4$, revealing that the chemical structure of g-$C_3N_4$ remains intact in the $Ag_3PO_4$/g-$C_3N_4$ composites.

The morphologies of $Ag_3PO_4$ nanocrystals, pure g-$C_3N_4$, and $Ag_3PO_4$/g-$C_3N_4$ composites were observed by SEM and TEM images, as shown in Fig. 2. Figure 2a showed the SEM image of $Ag_3PO_4$ crystals with diameter

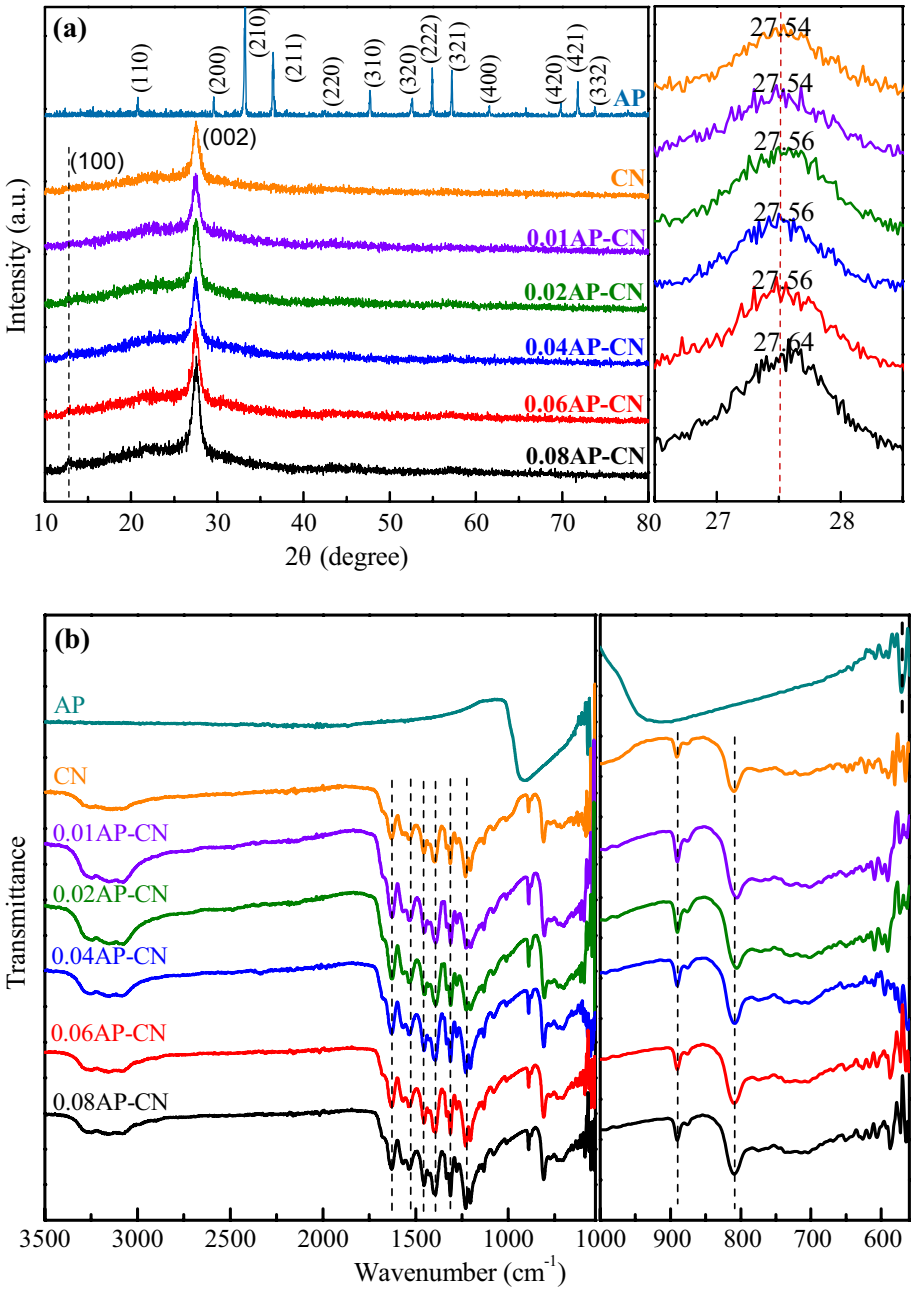


**Fig. 1** XRD patterns (**a**) and FTIR spectra (**b**) of $Ag_3PO_4$, the pure g-$C_3N_4$, and the $Ag_3PO_4$/g-$C_3N_4$ composites with variable $Ag_3PO_4$ contents (0.01 g, 0.02 g, 0.04 g, 0.06 g, and 0.08 g) mixed with 8 g urea

around 1 micrometer. SEM image for the pure g-$C_3N_4$, as shown in Fig. 2b, displayed the pure g-$C_3N_4$ are cotton-like flocculus aggregated by irregular nanosheets. The SEM image in Fig. 2c showed that the 0.04AP-CN sample remains a similar appearance compared with the pure g-$C_3N_4$. TEM images in Fig. 2d and e showed the overview of the $Ag_3PO_4$/g-$C_3N_4$ composite. The $Ag_3PO_4$ nanoparticles were randomly distributed among the g-$C_3N_4$ layers. A high magnification TEM image in Fig. 2f showed the AP particles with size around 20–30 nm were wrapped by graphitic carbon nitride layers. The size of $Ag_3PO_4$ particle is obvious smaller than that of pure $Ag_3PO_4$ microcystals, which split to smaller particle during the thermal annealing process with urea.

AFM was employed to further investigate the surface morphologies of the pure g-$C_3N_4$ and 0.04AP-CN. Samples were dispersed in ethanol by ultrasonic treatment and then dropped onto a silicon surface. AFM image, as shown in Fig. 3a, demonstrated that the pure g-$C_3N_4$ is composed of triangle plate with side length of around 500–800 nm. AFM image for 0.04AP-CN showed that $Ag_3PO_4$ nanoparticles distributed randomly on the surface of g-$C_3N_4$ layers. The line profile inserted in Fig. 3b showed that the thickness of g-$C_3N_4$ plates is about 6.5 nm, roughly about 20 layers of

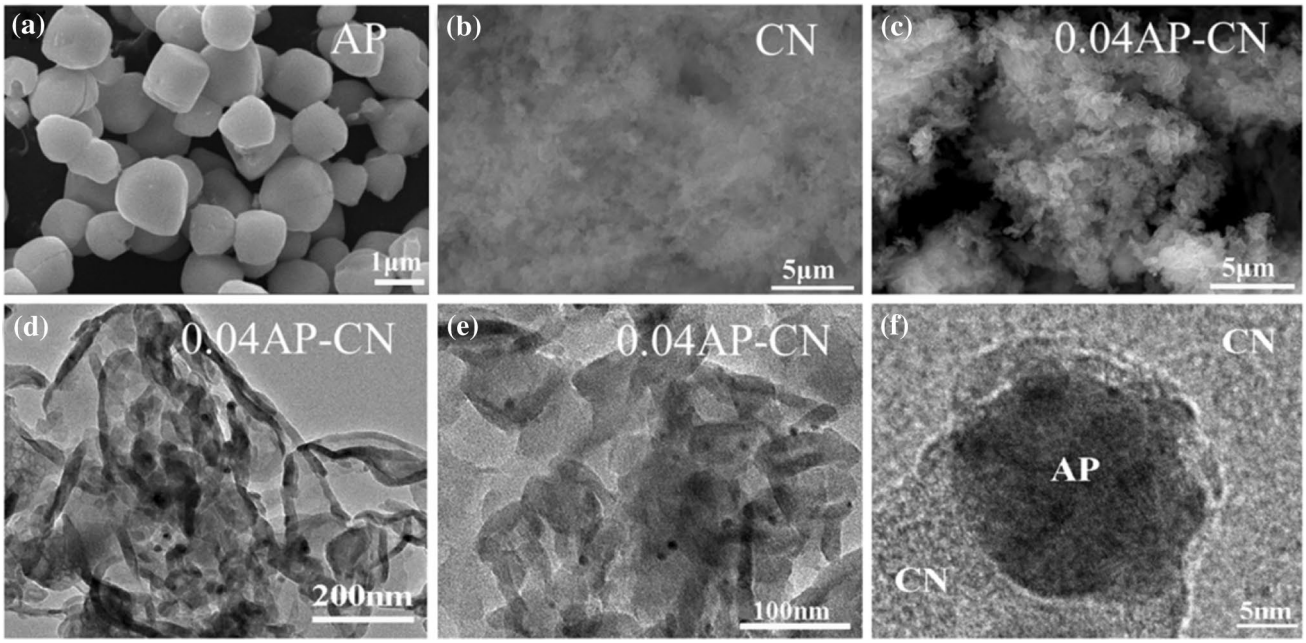


**Fig. 2** The SEM images of $Ag_3PO_4$ crystals (**a**), pure g-$C_3N_4$ (**b**), and 0.04AP-CN composite (**c**). TEM images of 0.04AP-CN nanocomposite with different magnifications (**d**)–(**f**)

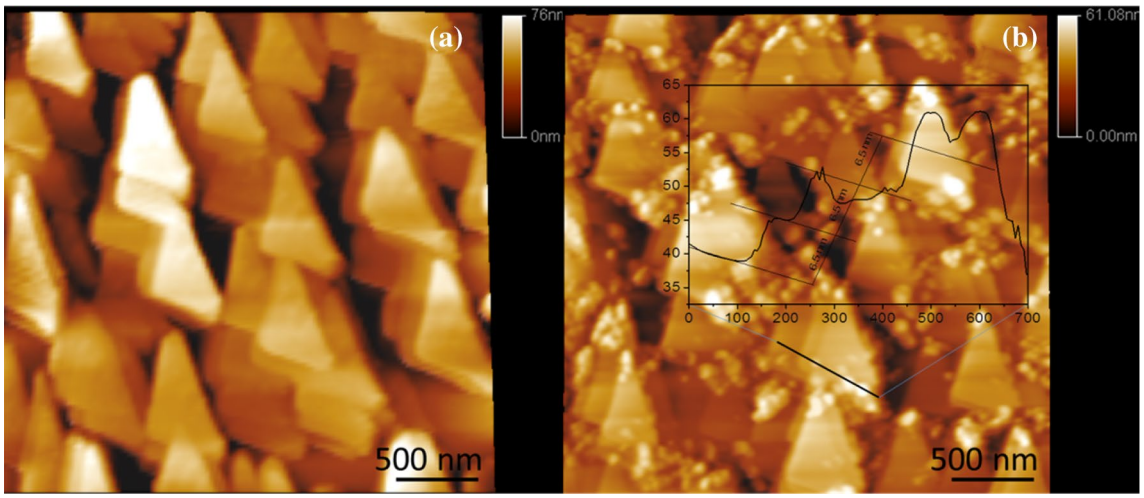


**Fig. 3** AFM images for the pure g-$C_3N_4$ and the $Ag_3PO_4$/g-$C_3N_4$ (0.04AP-CN) nanocomposites

g-$C_3N_4$, and the $Ag_3PO_4$ particle size is around 20–30 nm, which is consistent with TEM images.

Figure 4 showed the scan survey and the high-resolution XPS spectra of C, N, Ag, P and O elements for $Ag_3PO_4$, the pure g-$C_3N_4$, and the $Ag_3PO_4$/g-$C_3N_4$ composite. For the pure g-$C_3N_4$ sample, there are three sharp peaks at 286, 398, and 530 eV, which are assigned to C 1 s, N 1 s, and O 1 s signals, respectively. The $Ag_3PO_4$/g-$C_3N_4$ composite formed after mixing with $Ag_3PO_4$ appears one new peak positioned at 367 eV assigning to Ag 3d and another at 133 eV assigning to P 2p, as shown in the survey scan in Fig. 4a. The high-resolution C 1 s XPS spectra of the three samples were shown in Fig. 4b. For the pure g-$C_3N_4$ nanosheets, the peaks centered at about 287.9 eV (C1) is typically attributed to the $sp^2$ hybrid C atoms bonded to N-containing aromatic skeleton rings (N–C=N) coordination. The peak at 285.8 eV (C2) is attributed to C–$NH_2$ bonded in the triazine ring of the reactant intermediary product. The peak at 284.4 eV (C3) could be attributed to the graphite C = C and adventitious carbon. The N 1 s spectra for the pure g-$C_3N_4$ in Fig. 4c

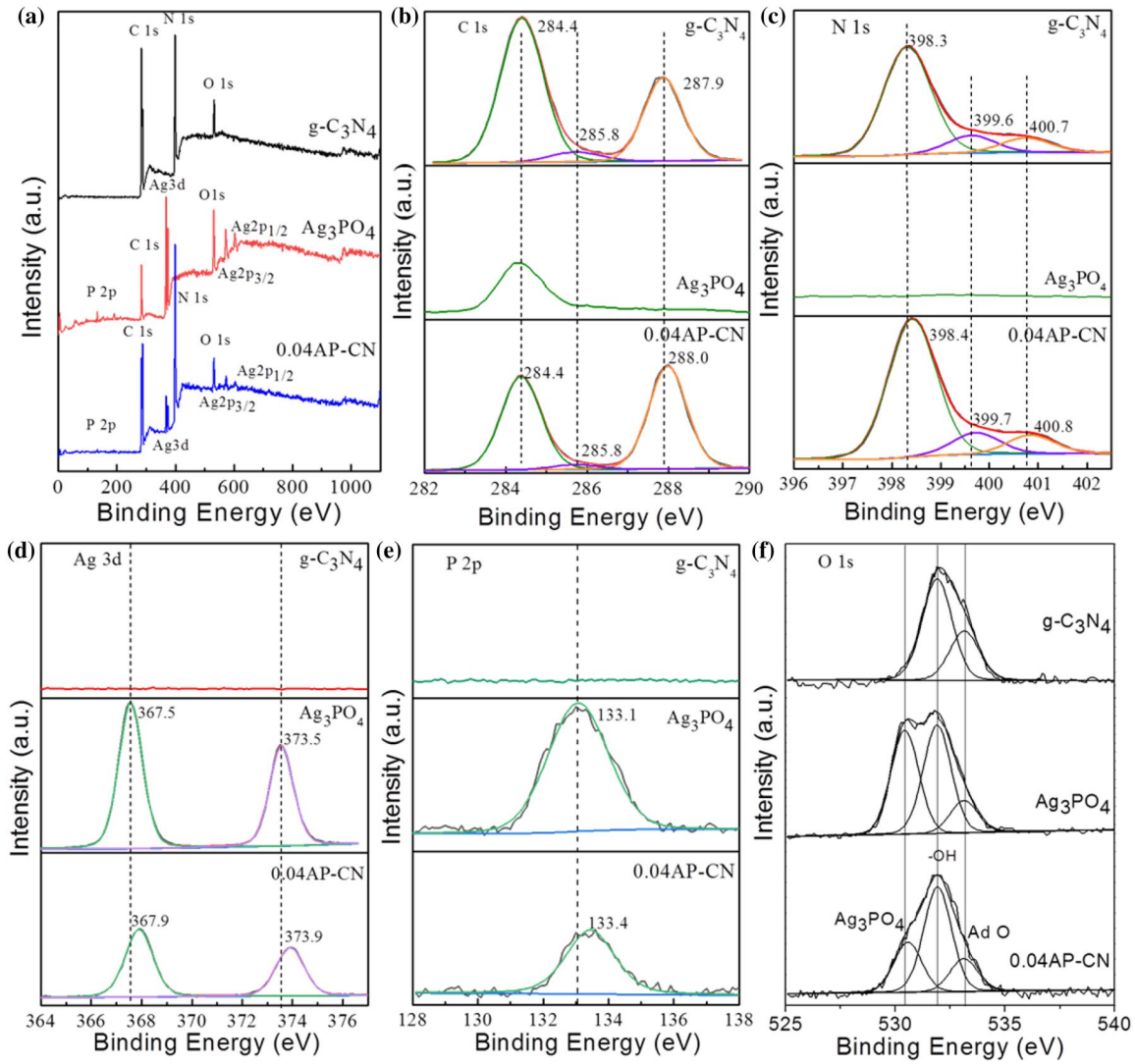


**Fig. 4** XPS survey scan (**a**) and high resolution spectra for C 1 s (**b**) and N 1 s (**c**), Ag 3d (**d**), P 2p (**e**), and O 1 s (**f**) for the pure g-$C_3N_4$ nanosheets (CN), $Ag_3PO_4$ nanoparticles (AP) and the $Ag_3PO_4$/g-$C_3N_4$ (0.04AP-CN) composites

can be mainly decomposed to three typical peaks located at about 398.3 eV (N1), 399.6 eV (N2), 400.7 eV (N3), which could be attributed to the $sp^2$-hybridized aromatic N atoms bonded to carbon atoms (C–N=C), and $sp^3$-hybridized N atoms of $N(–C)_3$ and terminal amino functions ($C–NH_2$), respectively [18–20]. The high resolution Ag 3d spectrum for $Ag_3PO_4$ in Fig. 4d showed that the peaks at 367.5 eV and 373.5 eV are attributed to $3d_{5/2}$ and $3d_{3/2}$ of $Ag^+$ in $Ag_3PO_4$. After forming the $Ag_3PO_4$/g-$C_3N_4$ composite, the peaks for $Ag^+$ still exist and shift to higher binding energy compared with the pure $Ag_3PO_4$, suggesting the presence of $Ag_3PO_4$ in the $Ag_3PO_4$/g-$C_3N_4$ composite [34]. The high resolution P 2p showed that the P 2p peak for the $Ag_3PO_4$/g-$C_3N_4$ composite shifts to higher binding energy side compared with that of pure $Ag_3PO_4$, implying that there exists electron interaction between $Ag_3PO_4$ and g-$C_3N_4$. The O 1 s spectrum for the pure g-$C_3N_4$ in Fig. 4f was fitted to two peaks at 531.7 and 532.9 eV, corresponding to the adsorbed –OH group and the adventitious $O_2$. After forming the $Ag_3PO_4$/g-$C_3N_4$ composite, a new peak at 530.3 eV appears, which is attributed to the O signal arising from $Ag_3PO_4$. Therefore, XPS results confirmed that there were both $Ag_3PO_4$ and g-$C_3N_4$ species in the composite structure. The binding energy shifts of those elements imply that there exists interaction in the interface by attracting electrons of both $Ag_3PO_4$ and g-$C_3N_4$ layer.

## 3.2 Photogenerated Charge Separation

To identify the electronic structure and photoelectric properties of the pure g-$C_3N_4$ and the $Ag_3PO_4$/g-$C_3N_4$ nanocomposite photocatalysts, UV–vis diffusion reflectance

spectroscopy and PL spectra were measured, as shown in Fig. 5a and b. The UV–vis absorbance spectra, as shown in Fig. 5a, demonstrated that the pure g-$C_3N_4$ absorbs light from UV through the visible range up to 465 nm, corresponding to band gap of 2.67 eV of the intrinsic absorption from valence to conduction band. The absorption edge of pure $Ag_3PO_4$ has a broader absorption in the visible region with an absorption edge at about 550 nm. The absorption edge of $Ag_3PO_4$/g-$C_3N_4$ composites displays a slightly red shift (~475.5 to ~485 nm) as the of $Ag_3PO_4$ content increased. The absorption edge for 0.01AP-CN, 0.02AP-CN, 0.04AP-CN, 0.06AP-CN, and 0.08AP-CN is 475.5 nm, 475.5 nm, 485.0 nm, 481.5 nm, and 485.0 nm, respectively. The corresponding band gap is 2.61 eV, 2.61 eV, 2.56 eV, 2.58 eV, and 2.56 eV, which is smaller than that of g-$C_3N_4$ and larger than that of $Ag_3PO_4$ (2.09 eV). Especially, the light absorption in the visible light range was enhanced significantly. The enhanced visible light absorption indicated that the composite photocatalysts could utilize more visible light, thus facilitate the photocatalytic reaction. Figure 5b showed the photoluminescence spectra of the pure g-$C_3N_4$ and $Ag_3PO_4$/g-$C_3N_4$ composites with different amount of $Ag_3PO_4$ under an excitation wavelength of 375 nm. Pure g-$C_3N_4$ shows a strong intrinsic emission band with a peak at 473.2 nm, which attributed the intrinsic emission of direct electron–hole recombination. With the increase of $Ag_3PO_4$ content, the PL intensity for AP-CN decreases at first, and 0.04AP-CN with lowest PL intensity. After that, the PL intensity increases a little with increase of $Ag_3PO_4$ content.

The specific surface area and pore size distribution of the prepared samples were obtained from $N_2$ absorption–desorption measurements, shown in Fig. 6. The specific surface area of 0.04AP-CN was calculated to be 137.1 $m^2$/g, larger than the 109.0 $m^2$/g of g-$C_3N_4$. The larger surface area

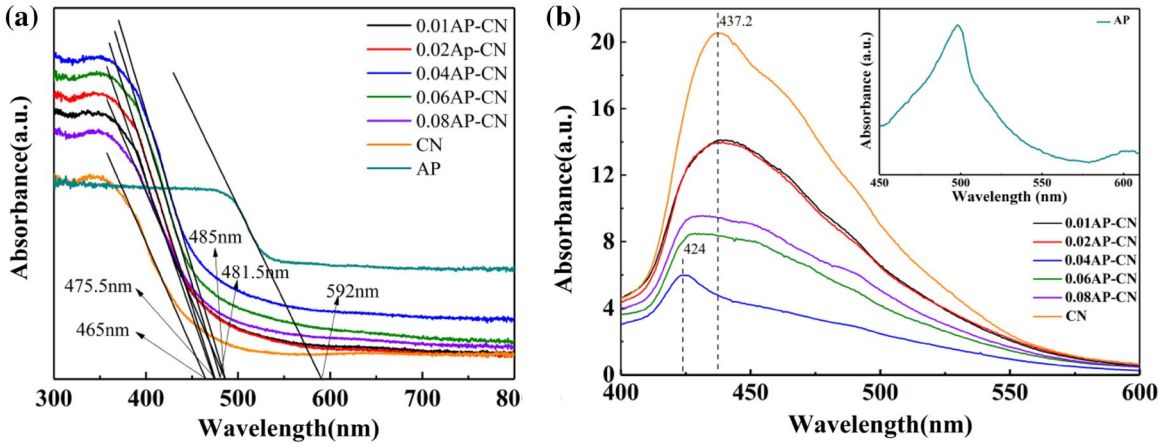


**Fig. 5** **a** UV–vis absorbance spectra, **b** PL spectra of $Ag_3PO_4$ (AP), the pure g-$C_3N_4$ nanosheets (CN) and the $Ag_3PO_4$/g-$C_3N_4$ (0.01AP-CN, 0.02AP-CN, 0.04AP-CN, 0.06AP-CN, and 0.08AP-CN) nanocomposites

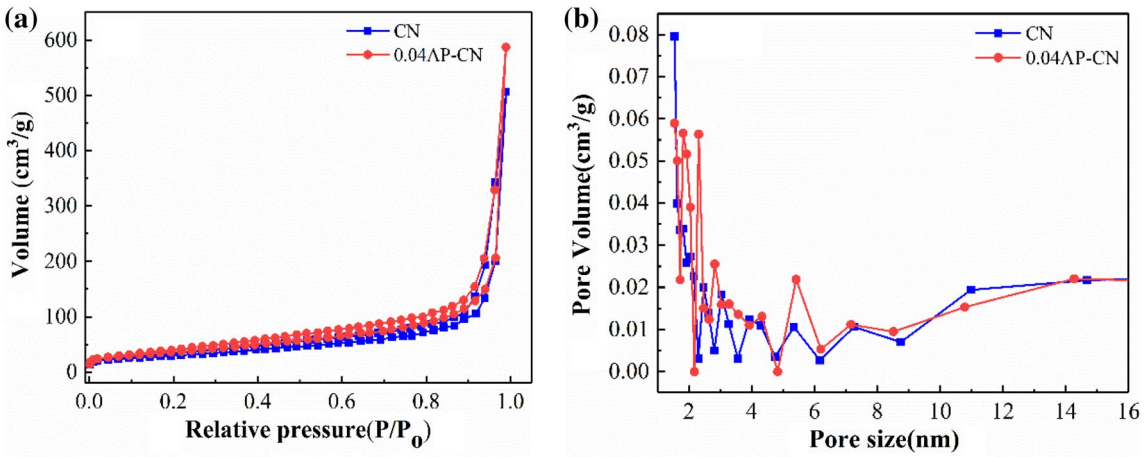


**Fig. 6** Nitrogen adsorption–desorption isotherms (**a**) and the corresponding pore-size distribution curves (**b**) for the pure g-$C_3N_4$ and 0.04AP-CN composite

for the 0.04AP-CN composite provides more active reaction sites during photocatalytic process, thus improves the photocatalytic performance. The pore distribution (Fig. 6b) showed the size of mesopores is in the range of 1–6 nm. The small pores existed in the 0.04AP-CN composite contribute to improve the photocatalytic performance.

The transient photocurrent responses of the pure g-$C_3N_4$ and the $Ag_3PO_4$/g-$C_3N_4$ composites under visible light were recorded in Fig. 7a. The photocurrent for the $Ag_3PO_4$/g-$C_3N_4$ composite showed a gradual attenuation at the initial 400 s period upon switching on light, which demonstrated the composites showed obvious photocorrossion phenomenon. The photocurrent tends to level stable for prolonged light irradiation. The spike-like shape of photocurrent transients is indicating of surface recombination process going on. A rapid decay is observed after initial rise, which is ascribed to the accumulation of photoinduced holes, rendering its combination with the photoinduced electrons [35–37]. The pure g-$C_3N_4$ photocatalyst reached at a stable photocurrent under visible light irradiation without photocorrosion occuring. The current density for 0.04AP-CN is the highest among all the composites, which is about 3 times of that observed for the pure g-$C_3N_4$ sample, revealing the most effective separation and transition of photoinduced electron/hole pairs, which is consistent with PL spectra.

The electrochemical impedance spectra (EIS) of the pure g-$C_3N_4$ and the $Ag_3PO_4$/g-$C_3N_4$ composites were measured to understand the photocatalytic mechanism. The arc on the EIS Nyquist plot indicates the charge transfer resistance. Generally speaking, the smaller of arc radius is, the lower of the charge transfer resistance will be [21, 24]. As shown in Fig. 7b, the Nyquist plots of all the $Ag_3PO_4$/g-$C_3N_4$ samples demonstrate smaller arc radius attributing to the reduced electronic resistance and increased electronic conductivity by hybridization $Ag_3PO_4$ with the pure g-$C_3N_4$. Similarly, the arc radius for 0.04AP-CN is smallest in all samples, which is associated with the highest efficiency of the charge separation [38–40]. Moreover, it is vital that the change trend of the arc radius for g-$C_3N_4$ samples is roughly consistent with the results displayed in PL spectra.

### 3.3 Photocatalytic Activity for $H_2$ Evolution

The photocatalytic performance of the prepared samples was evaluated with $H_2$ production with 20 wt% TEOA as sacrificial electron donor and without Pt ion co-catalyst under visible light irradiation, as shown in Fig. 8a. The photocatalytic $H_2$ evolution rate for 0.01AP-CN, 0.02AP-CN, 0.04AP-CN, 0.06AP-CN, and 0.08AP-CN is recorded as 4.63, 5.21, 8.93, 6.08, 3.27 μmol/h, respectively, which are all higher than that of pure g-$C_3N_4$ with 2.67 μmol/h. These results clearly demonstrate the photocatalytic activity of the $Ag_3PO_4$/g-$C_3N_4$ composites have been significantly improved by introducing trace amount of $Ag_3PO_4$ nanoparticles to form the $Ag_3PO_4$/g-$C_3N_4$ composites. The 0.04AP-CN photocatalyst has the most favorable photocatalytic activity with an average $H_2$ evolution rate of among all $Ag_3PO_4$/g-$C_3N_4$ composites, which is 3.3 times as high as that of pure g-$C_3N_4$. The composites loading $Ag_3PO_4$ beyond that of the 0.04AP-CN sample nevertheless exhibit weaker photocatalytic performance, which is attributed that loading excessive $Ag_3PO_4$ nanoparticles may shield the g-$C_3N_4$ surface active sites. It is interesting that $Ag_3PO_4$/g-$C_3N_4$ composites have good photocatalytic $H_2$ evolution rate even at a condition of without Pt ion co-catalyst. The stability of $H_2$ evolution for 0.04AP-CN was tested four round photocatalytic experiments under same condition (Fig. 8b). The $H_2$ evolution remains unchanged under four runs of photocatalytic reaction, which demonstrated the composite photocatalyst are basically stable. In order to explore the effect of

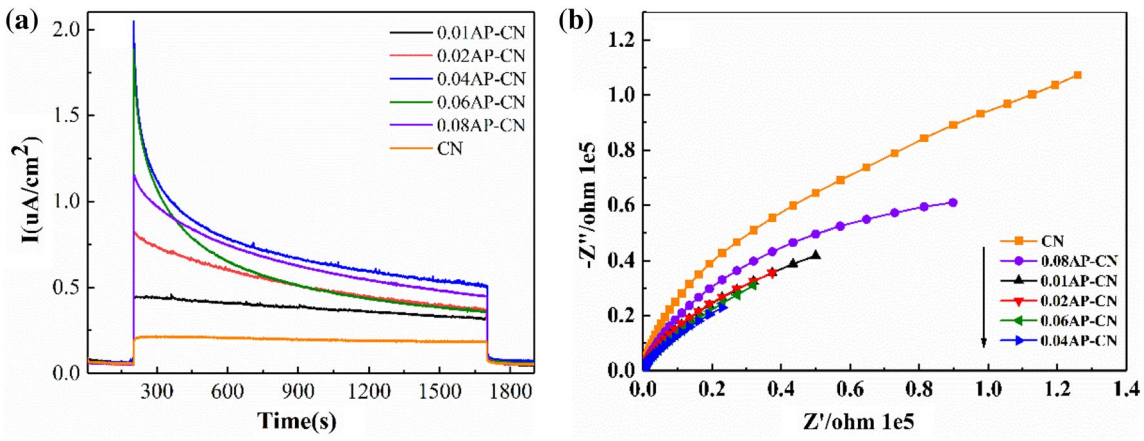


**Fig. 7** Transient photocurrents (**a**) and EIS (**b**) spectra of the pure g-$C_3N_4$ nanosheets (CN) and the $Ag_3PO_4$/g-$C_3N_4$ (0.01AP-CN, 0.02AP-CN, 0.04AP-CN, 0.06AP-CN, and 0.08AP-CN) nanocomposites

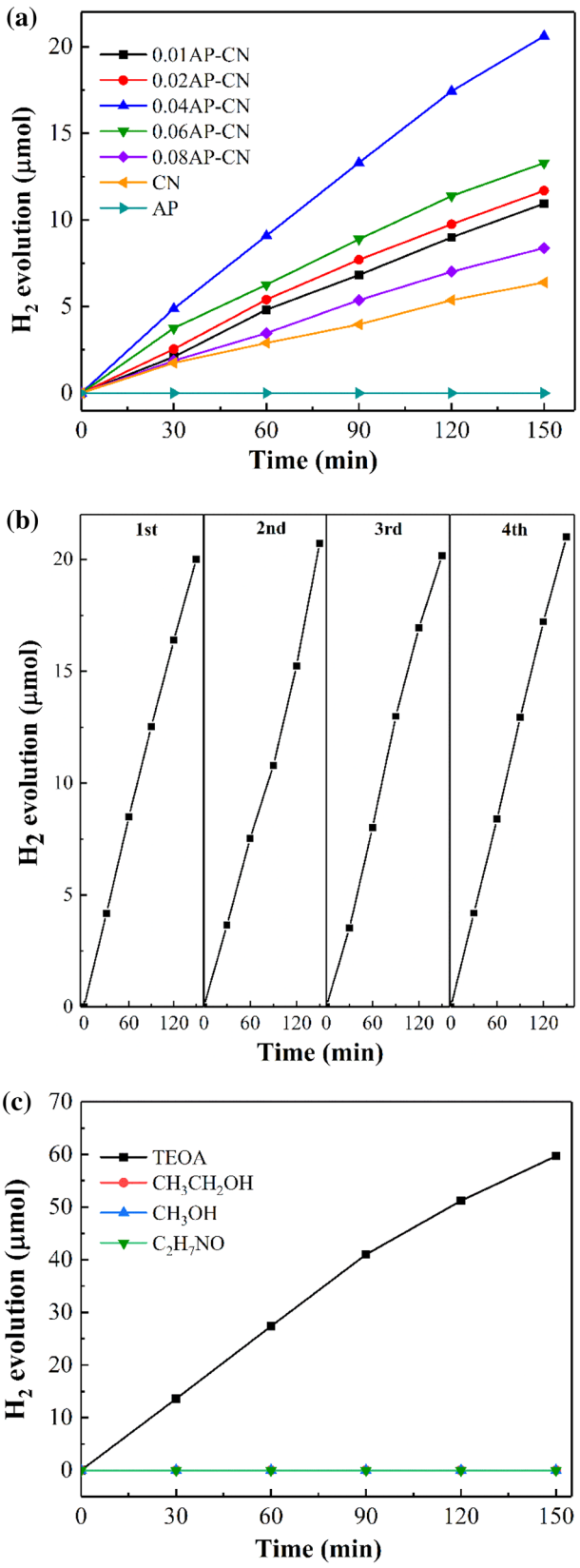


**Fig. 8** Photocatalutic $H_2$ evolution of the $Ag_3PO_4$/g-$C_3N_4$ composites with different $Ag_3PO_4$ contents (**a**) and stability of 0.04AP-CN (**b**) with 20 vol% TEOA, 0 wt% Pt, and 10 mg photocatalysts under visible light irradiation ($\lambda > 400$ nm). (**c**) Photocatalytic $H_2$ evolution of 0.04AP-CN with different sacrificial electron donors

different sacrificial hole reagents on the photocatalytic performance, the photocatalytic $H_2$ evolution rate for 0.04AP-CN was measured using TEOA, ethanol ($CH_3CH_2OH$), methanol ($CH_3OH$), and ethanolamine ($C_2H_7NO$), as shown in Fig. 8c. Only TEOA can act as an efficient sacrificial reagent in the water splitting process, and the $H_2$ evolution is very stable.

In the condition with 20 vol% TEOA and 3 wt% Pt, the photocatalytic $H_2$ evolution rate increased dramatically, but in different degrees, as shown in Fig. 9a, compared with that of without Pt co-catalyst. The $H_2$ evolution rate for the pure g-$C_3N_4$, 0.01AP-CN, 0.02AP-CN, 0.04AP-CN, 0.06AP-CN, and 0.08AP-CN is 11.44, 10.70, 13.80, 27.36, 14.73, and 4.84 μmol/h respectively. The 0.04AP-CN has the highest increase rate among all the $Ag_3PO_4$/g-$C_3N_4$ composite photocatalysts, and the pure g-$C_3N_4$ has the second highest increase rate compared with the values in Fig. 8a. For the AP-CN composites, Ag particles acted as co-catalyst may have occupied some active sites of g-$C_3N_4$. In contrast, the pure g-$C_3N_4$ have more active sites for Pt co-catalyst. Therefore, g-$C_3N_4$ has higher hydrogen evolution rate than other AP-CN composites. The photocatalytic performance for AP-CN composites is consistent with the charge transfer properties. The photocatalytic $H_2$ evolution rate for 0.04AP-CN is as 2.14 times as that of the pure g-$C_3N_4$. The $H_2$ evolution tests in Figs. 8a and 9a showed that $Ag_3PO_4$ cannot produce $H_2$ under visible light irradiation. The $Ag_3PO_4$/g-$C_3N_4$ composite formed by wrapping $Ag_3PO_4$ nanopaticles with g-$C_3N_4$ layer can produce $H_2$ via water splitting by improve the separation of photoinduced charge carriers and increase the visible light absorption. Figure 9b showed the photocatalytic performance of 0.04AP-CN with 0 wt% and 3 wt% Pt co-catalyst. The 0.04AP-CN sample can produce $H_2$ continually during 7 h visible light irradiation. Even if at the condition of without Pt co-catalyst, 0.04AP-CN keeps photocatalytic vitality and produce $H_2$ under visible light irradiation for 7 h. The $H_2$ production increases dramatically with 3 wt% Pt co-catalyst. Table 1 shows the $H_2$ evolution rate (HER) and AQY (%) of the $Ag_3PO_4$/g-$C_3N_4$ composites with TEOA as sacrificial regent and 0 wt%, 3 wt% Pt under visible light irradiation.

### 3.4 Discussion on Mechanism

After 150 min of visible light irradiation, the 0.04AP-CN catalyst was retrieved by centrifugation and a subsequent drying process. XPS was used to analyze its chemical

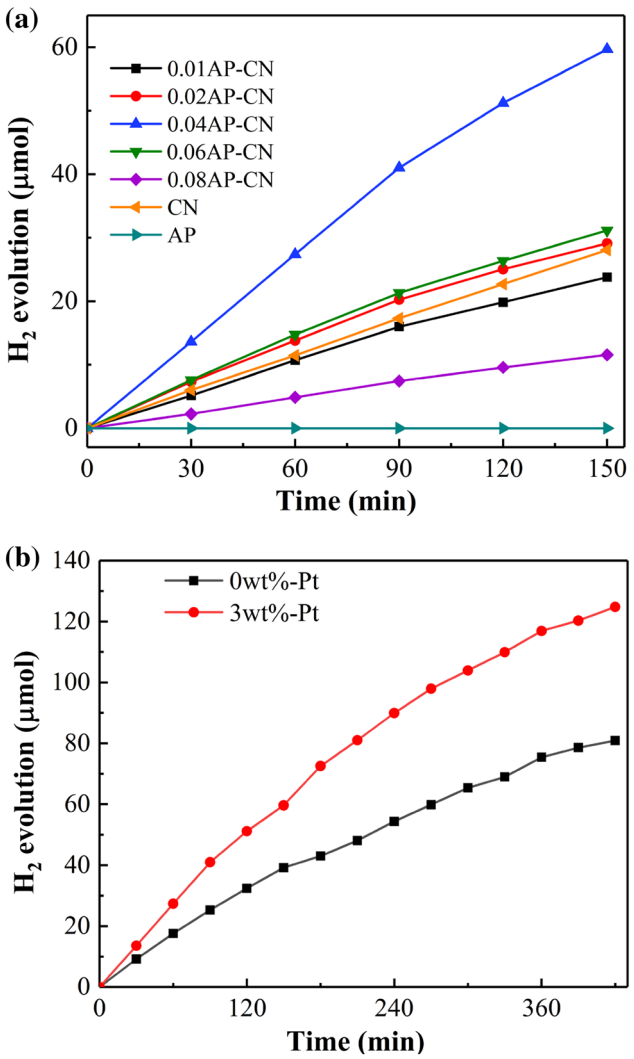


**Fig. 9** **a** Photocatalutic $H_2$ evolution of the $Ag_3PO_4$/g-$C_3N_4$ composites with different $Ag_3PO_4$ contents with 20 vol% TEOA, 3 wt% Pt, and 10 mg photocatalysts under visible light irradiation ($\lambda > 400$ nm). **b** Photocatalytic $H_2$ evolution rates of 0.04AP-CN with 0 wt% and 3 wt% Pt co-catalyst

**Table 1** The $H_2$ evolution rate and AQY (%) of $Ag_3PO_4$/g-$C_3N_4$ composites with TEOA as an electron donor and 0 wt%, 3 wt% Pt under visible light irradiation

| Sample | HER [μmol/(g·h)] with 20 vol% TEOA and 0 wt% Pt | AQY (%) | HER [μmol/(g·h)] with 20 vol% TEOA and 3 wt% Pt | AQY (%) |
|---|---|---|---|---|
| AP | 0 | 0 | 0 | 0 |
| CN | 267 | 1.46 | 1144 | 6.27 |
| 0.01AP-CN | 463 | 2.54 | 1070 | 5.87 |
| 0.02AP-CN | 521 | 2.86 | 1380 | 7.56 |
| 0.04AP-CN | 893 | 4.90 | 2736 | 10.22 |
| 0.06AP-CN | 608 | 3.33 | 1473 | 8.07 |
| 0.08AP-CN | 327 | 1.79 | 484 | 2.65 |

composition changes under visible light irradiation. The XPS analysis in Fig. 10 showed that the spectra of C 1 s, N 1 s, and P 2p remain unchanged. In the Ag 3d spectrum, two new peaks at binding energy of 366.8 eV and 372.7 eV can be ascribed to Ag $3d_{5/2}$ and $3d_{3/2}$ of $Ag^0$ atoms, while the other two peaks at 367.8 eV and 373.8 eV corresponded to Ag $3d_{5/2}$ and $3d_{3/2}$ of $Ag^+$ in $Ag_3PO_4$. A new peak at 529.3 eV in the O 1 s spectrum can be ascribed to the oxygen bonded to the surface of Ag particles. The XPS results demonstrated that $Ag_3PO_4$ particles underwent partially decomposing to Ag particles under visible light irradiation, nevertheless, the g-$C_3N_4$ remained intact.

Ultraviolet photoelectron spectroscopy (UPS) was employed to measure the valence band and the conduction band of the $Ag_3PO_4$/g-$C_3N_4$ composite, shown in Fig. 11a. The valence band ($E_v$) energy of g-$C_3N_4$, $Ag_3PO_4$, and the $Ag_3PO_4$/g-$C_3N_4$ composite is determined to be 6.57 eV, 6.67 eV, and 6.97 eV by substracting the width of the He I UPS spectra from the excitation energy (21.22 eV). The conduction band ($E_c$) energy is thus estimated at 3.90 eV, 4.58 eV, and 4.41 eV for the pure g-$C_3N_4$, $Ag_3PO_4$, and 0.04AP-CN, respectively. The $E_g$, $E_v$, and $E_c$ values of g-$C_3N_4$, $Ag_3PO_4$, and 0.04AP-CN are converted to electrochemical potentials in volts according to the reference standard for which 0 V versus reversible hydrogen electrode (RHE) equals $^-$4.44 eV versus vacuum level. Figure 11b showed the proposed band structure diagram of heterojunction for the $Ag_3PO_4$/g-$C_3N_4$ composite. The reduction level for $H_2$ is positioned below the conduction band of the $Ag_3PO_4$/g-$C_3N_4$ composite. These bands are properly positioned to permit the transfer of electrons and holes for water splitting. The enhanced photocatalytic performance could be attributed to the improved separation of photoinduced charge carriers at the interface between $Ag_3PO_4$ and g-$C_3N_4$. The PL, EIS and photocurrent results showed that the separation of photoinduced electron–hole pairs was improved obviously after introducing a trace amount of $Ag_3PO_4$ to form the $Ag_3PO_4$/g-$C_3N_4$ hybrid composite, in which Ag nanoparticles at the interface of $Ag_3PO_4$/g-$C_3N_4$ act as the charge separation center to form the visible light driven Z-scheme system. With energy higher than the band gap in g-$C_3N_4$ and $Ag_3PO_4$, photoinduced electrons jump into CB and leave holes in VB. Ag nanoparticles were formed under visible light irradiation. The CB potential of $Ag_3PO_4$ is more negative than the Fermi level of metallic Ag, and the VB potential of g-$C_3N_4$ is more positive than the Fermi level of Ag. The phtotoinduced electrons in CB of $Ag_3PO_4$ could easily shift into Ag nanoparticles because of the more positive Fermi energy of Ag than the CB level of $Ag_3PO_4$. Synchronously, the holes in the VB of g-$C_3N_4$ can also shift into Ag nanoparticles due to the more negative Fermi energy of Ag than the VB level of g-$C_3N_4$. In the photocatalytic process, Ag nanoparticles at the interface act as the recombination

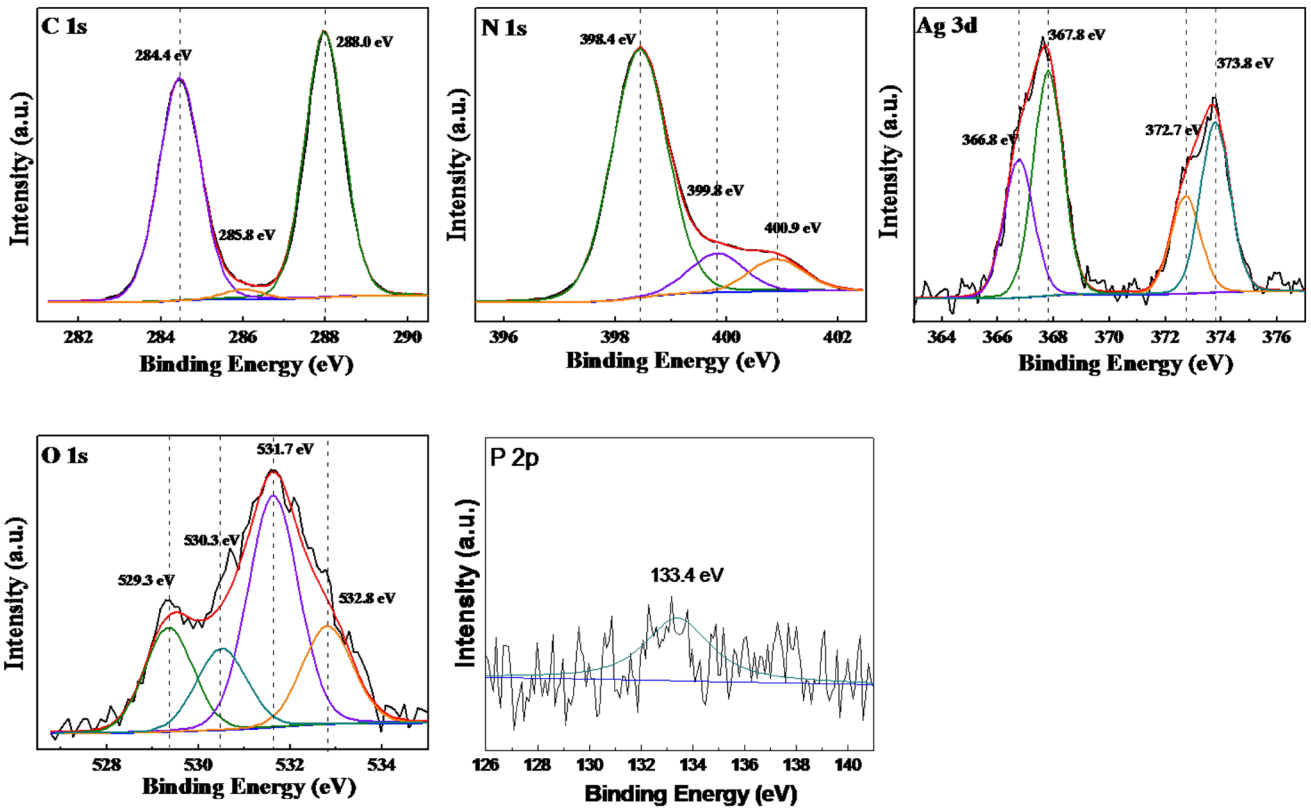


**Fig. 10** XPS spectra for C 1 s, N 1 s, Ag 3d, O 1 s, and P 2p for the 0.04AP-CN photocatalyst after visible light irradiation of 150 min

center for the electrons from the CB of $Ag_3PO_4$ and holes from VB of g-$C_3N_4$. Thus the photoinduced electrons hold back at the CB of g-$C_3N_4$, and photoinduced holes at the VB of $Ag_3PO_4$, enhancing the separation of the photoinduced electrons and holes. The electrons in CB of g-$C_3N_4$ is more negative, with strong reduction power, which is responsible for the enhanced photocatalytic efficiency of water splitting [30–32].

## 4 Conclusion

In summary, the $Ag_3PO_4$/g-$C_3N_4$ nanocomposites were successfully prepared by a facile calcination method by one-pot calcining the mixture of $Ag_3PO_4$ and urea. Trace $Ag_3PO_4$ introduced in the composite photocatalysts enhanced the photocatalytic $H_2$ evolution rate under visible light irradiation. 0.04AP-CN photocatalyst showed highest photocatalytic $H_2$ evolution rate of 27.36 μmol/h with 3 wt% Pt ion and 8.93 μmol/h without co-catalyst. Compared to the pure g-$C_3N_4$ nanosheets, the photocatalytic $H_2$ evolution rate increases 3.34 times without Pt co-catalyst, and 2.39 times with 3 wt% Pt co-catalyst. The experimental results showed that the synergistic effect of the interface between $Ag_3PO_4$ and g-$C_3N_4$ resulted in the improved separation of photoinduced charge carriers and enhanced absorption in the visible light region.

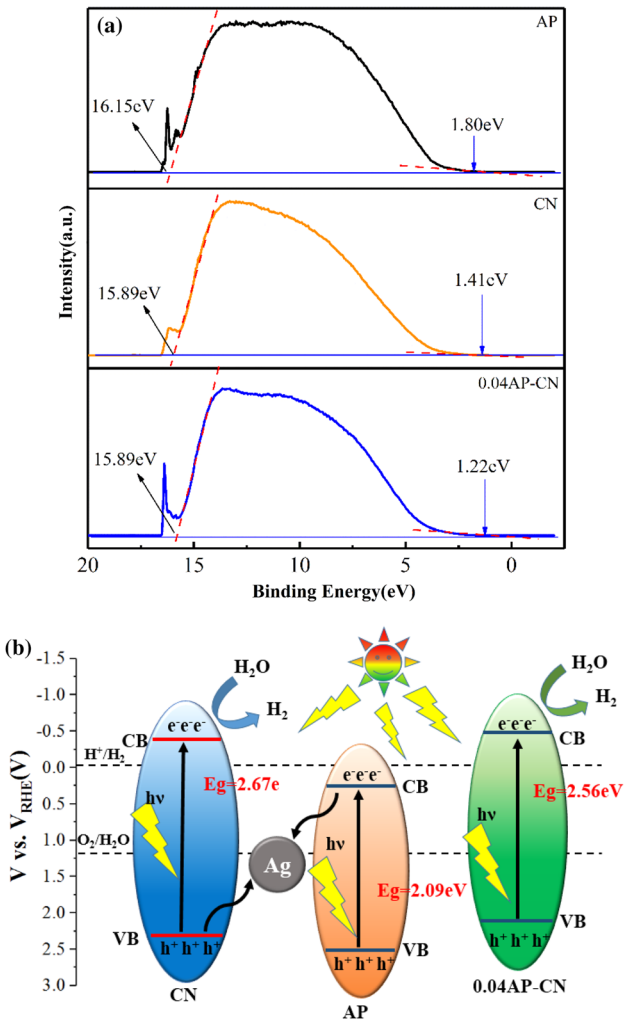


**Fig. 11** **a** UPS spectra of $Ag_3PO_4$, pure g-$C_3N_4$, and 0.04AP-CN nanocomposite. **b** Proposed band structure diagram of heterojunction for the $Ag_3PO_4$/g-$C_3N_4$ composite

**Acknowledgements** This work was financially supported by the National Natural Science Foundation of China (Grant Nos. 21173170, 51801164).

**Author Contributions** The manuscript was written through contributions of all authors. All authors have given approval to the final version of the manuscript.

## Compliance with Ethical Standards

**Conflict of interest** The authors declare no competing financial interest.

## References

1. Liu C, Tang J, Chen HM, Liu B, Yang P (2013) A fully integrated nanosystem of semiconductor nanowires for direct solar water splitting. Nano Lett 13:2989–2992
2. Hisatomi T, Kubota J, Domen K (2014) Recent advances in semiconductors for photocatalytic and photoelectrochemical water splitting. Chem Soc Rev 43:7520–7535
3. Liu B, Wu CH, Miao JW, Yang PD (2014) All inorganic semiconductor nanowire mesh for direct solar water splitting. ACS Nano 8:11739–11744
4. Cui YJ (2015) In-situ synthesis of $C_3N_4$/CdS composites with enhanced photocatalytic properties. Chin J Catal 36:372–379
5. Liu G, Wang T, Zhang H, Meng X, Hao D, Chang K, Li P, Kako T, Ye J (2015) Nature-Inspired environmental "phosphorylation" boosts photocatalytic $H_2$ production over carbon nitride nanosheets under visible-light irradiation. Angew Chem Int Ed Engl 54:13561–13565
6. Wu P, Wang J, Zhao J, Guo L, Osterloh FE (2014) High alkalinity boosts visible light driven $H_2$ evolution activity of g-$C_3N_4$ in aqueous methanol. Chem Commun 50:15521–15524
7. Niu P, Zhang L, Liu G, Cheng H-M (2012) Graphene-like carbon nitride nanosheets for improved photocatalytic activities. Adv Funct Mater 22:4763–4770
8. Dou H, Chen L, Zheng S, Zhang Y, Xu GQ (2018) Band structure engineering of graphitic carbon nitride via $Cu^{2+}$/$Cu^{+}$ doping for enhanced visible light photoactivity. Mate Chem Phys 214:482–488
9. Liu E, Chen J, Ma Y, Feng J, Jia J, Fan J, Hu X (2018) Fabrication of 2D $SnS_2$/g-$C_3N_4$ heterojunction with enhanced $H_2$ evolution during photocatalytic water splitting. J Colloid Interface Sci 524:313–324
10. Pan C, Xu J, Wang Y, Li D, Zhu Y (2012) Dramatic activity of $C_3N_4$/$BiPO_4$ photocatalyst with core/shell structure formed by Self-assembly. Adv Funct Mater 22:1518–1524
11. Wang X, Zhang L, Lin H, Nong Q, Wu Y, Wu T, He Y (2014) Synthesis and characterization of a $ZrO_2$/g-$C_3N_4$ composite with enhanced visible-light photoactivity for rhodamine degradation. RSC Adv 4:40029–40035
12. He K, Xie J, Liu ZQ, Li N, Chen X, Hu J, Li X (2018) Multifunctional $Ni_3C$ cocatalyst/g-$C_3N_4$ nanoheterojunctions for robust photocatalytic $H_2$ evolution under visible light. J Mater Chem A 6:13110–13122
13. Bi L, Xu D, Zhang L, Lin Y, Wang D, Xie T (2015) Metal Ni-loaded g-$C_3N_4$ for enhanced photocatalytic $H_2$ evolution activity: the change in surface band bending. Phys Chem Chem Phys 17:29899–29905
14. Ren HT, Jia SY, Wu Y, Wu SH, Zhang TH, Han X (2014) Improved photochemical reactivities of $Ag_2O$/g-$C_3N_4$ in phenol degradation under UV and visible light. Ind Eng Chem Res 53:17645–17653
15. Yan H, Yang H (2011) $TiO_2$-g-$C_3N_4$ composite materials for photocatalytic $H_2$ evolution under visible light irradiation. J Alloys Compd 509:L26–L29
16. Wei H, McMaster WA, Tan JZY, Chen D, Caruso RA (2018) Tricomponent brookite/anatase $TiO_2$/g-$C_3N_4$ heterojunction in mesoporous hollow microspheres for enhanced visible-light photocatalysis. J Mater Chem A 6:7236–7245
17. Chai B, Peng T, Mao J, Li K, Zan L (2012) Graphitic carbon nitride (g-$C_3N_4$)-Pt-$TiO_2$ nanocomposite as an efficient photocatalyst for hydrogen production under visible light irradiation. Phys Chem Chem Phys 14:16745–16752
18. Xu H, Yan J, Xu Y, Song Y, Li H, Xia J, Huang C, Wan H (2013) Novel visible-light-driven AgX/graphite-like $C_3N_4$ (X =

Br, I) hybrid materials with synergistic photocatalytic activity. Appl Catal B 129:182–193
19. Wang W, Yu JC, Xia D, Wong PK, Li Y (2013) Graphene and g-$C_3N_4$ nanosheets cowrapped elemental alpha-sulfur as a novel metal-free heterojunction photocatalyst for bacterial inactivation under visible-light. Environ Sci Technol 47:8724–8732
20. Hu S, Qu X, Li P, Wang F, Li Q, Song L, Zhao Y, Kang X (2018) Photocatalytic oxygen reduction to hydrogen peroxide over copper doped gaphitic carbon nitride hollow microsphere: the effect of Cu(I)-N active sites, Chem. Engineering J 334:410–418
21. Dou H, Zheng S, Zhang Y (2017) Graphitic carbon nitride with S and Fe(III) codoping for improved photodegradation performance. Catal Lett 148:601–611
22. Chen F, Yang Q, Wang Y, Zhao J, Wang D, Li X, Guo Z, Wang H, Deng Y, Niu C, Zeng G (2017) Novel ternary heterojunction photcocatalyst of Ag nanoparticles and g-$C_3N_4$ nanosheets co-modified $BiVO_4$ for wider spectrum visible-light photocatalytic degradation of refractory pollutant. Appl Catal B 205:133–147
23. Wang X, Yan J, Ji H, Chen Z, Xu Y, Huang L, Zhang Q, Song Y, Xu H, Li H (2016) MO degradation by Ag-$Ag_2O$/g-$C_3N_4$ composites under visible-light irradation. Springerplus 5:369
24. Zhou T, Xu Y, Xu H, Wang H, Da Z, Huang S, Ji H, Li H (2014) In situ oxidation synthesis of visible-light-driven plasmonic photocatalyst Ag/AgCl/g-$C_3N_4$ and its activity. Ceram Int 40:9293–9301
25. Bi Y, Ouyang S, Umezawa N, Cao J, Ye J (2011) Facet effect of single-crystalline $Ag_3PO_4$ sub-microcrystals on photocatalytic properties. J Am Chem Soc 133:6490–6492
26. Hou Y, Zuo F, Ma Q, Wang C, Bartels L, Feng P (2012) $Ag_3PO_4$ Oxygen Evolution Photocatalyst Employing Synergistic Action of Ag/AgBr Nanoparticles and Graphene Sheets. J Phy Chem C 116:20132–20139
27. He P, Song L, Zhang S, Wu X, Wei Q (2014) Synthesis of g-$C_3N_4$/$Ag_3PO_4$ heterojunction with enhanced photocatalytic performance. Mater Res Bull 51:432–437
28. Kumar S, Surendar T, Baruah A, Shanker V (2013) Synthesis of a novel and stable g-$C_3N_4$–$Ag_3PO_4$ hybrid nanocomposite photocatalyst and study of the photocatalytic activity under visible light irradiation. J Mater Chem A 1:5333
29. Ren Y, Zhao Q, Li X, Xiong W, Tade M, Liu L (2014) 2D Porous graphitic $C_3N_4$ nanosheets/$Ag_3PO_4$ nanocomposites for enhanced visible-light photocatalytic degradation of 4-chlorophenol. J Nanopart Res 16:2532
30. Jiang D, Zhu J, Chen M, Xie J (2014) Highly efficient heterojunction photocatalyst based on nanoporous g-$C_3N_4$ sheets modified by $Ag_3PO_4$ nanoparticles: synthesis and enhanced photocatalytic activity. J Colloid Interface Sci 417:115–120
31. He Y, Zhang L, Teng B, Fan M (2015) New application of Z-scheme $Ag_3PO_4$/g-$C_3N_4$ composite in converting $CO_2$ to fuel. Environ Sci Technol 49:649–656
32. Yang X, Tang H, Xu J, Antonietti M, Shalom M (2015) Silver phosphate/graphitic carbon nitride as an efficient photocatalytic tandem system for oxygen evolution. Chem Sus Chem 8:1350–1358
33. Cummings CY, Marken F, Peter LM, Tahir AA, Wijayantha KG (2012) Kinetics and mechanism of light-driven oxygen evolution at thin film alpha-$Fe_2O_3$ electrodes. Chem Commun 48:2027–2029
34. Zhong DK, Gamelin DR (2010) Photoelectrochemical water oxidation by cobalt catalyst ("Co-Pi")/alpha-$Fe_2O_3$ composite photoanodes: oxygen evolution and resolution of a kinetic bottleneck. J Am Chem Soc 132:4202–4207
35. Bledowski M, Wang L, Ramakrishnan A, Khavryuchenko OV, Khavryuchenko VD, Ricci PC, Strunk J, Cremer T, Kolbeck C, Beranek R (2011) Visible-light photocurrent response of $TiO_2$-polyheptazine hybrids: evidence for interfacial charge-transfer absorption. Phys Chem Chem Phys 13:21511–21519
36. Li J, Shen B, Hong Z, Lin B, Gao B, Chen Y (2012) A facile approach to synthesize novel oxygen-doped g-$C_3N_4$ with superior visible-light photoreactivity. Chem Commun 48:12017–12019
37. Lin L, Ren W, Wang C, Asiri AM, Zhang J, Wang X (2018) Crystalline carbon nitride semiconductors prepared at different temperatures for photocatalytic hydrogen production. Appl Catal B 231:234–241
38. Zhu Y, Ren J, Yang X, Chang G, Bu Y, Wei G, Han W, Yang D (2017) Interface engineering of 3D $BiVO_4$/Fe-based layered double hydroxide core/shell nanostructures for boosting photoelectrochemical water oxidation. J Mater Chem A 5:9952–9959
39. Dou H, Long D, Zheng S, Zhang Y (2018) A facile approach to synthesize graphitic carbon nitride microwires for enhanced photocatalytic $H_2$ evolution from water splitting under full solar spectrum. Catal Sci Technol 8:3599–3609
40. Li T, He Y, Cai J, Lin H, Luo M, Zhao L (2013) Preparation and characterization of Ag-loaded $SmVO_4$ for photocatalysis application. Photochem Photobiol 89:529–535